Forward modeling of ice topography on Mars to infer basal shear stress conditions

M. E. Banks[1] and J. D. Pelletier[1]

Received 15 January 2007; revised 13 April 2007; accepted 15 June 2007; published 1 January 2008.

[1] Understanding the history of ice caps on Mars could reveal important information about Martian geologic and climatic history. To do this, an ice reconstruction model is needed that operates over complex topography and can be constrained with a limited number of free parameters. In this study we developed a threshold-sliding model for ice cap morphology based on the classic model of Nye later incorporated into the models of Reeh and colleagues. We have updated the Nye-Reeh model with a new numerical algorithm. Although the model was originally developed to model perfectly plastic deformation, it is applicable to any ice body that deforms when a threshold basal shear stress is exceeded. The model requires three inputs: a digital elevation model of bed topography, a ''mask'' grid that defines the position of the ice terminus, and a function defining the threshold basal shear stress. To test the robustness of the model, the morphology of the Greenland ice sheet is reconstructed using an empirical equation between threshold basal shear stress and ice surface slope. The model is then used to reconstruct the morphology of ice draping impact craters on the margins of the south polar layered deposits using an inferred constant basal shear stress of $\sim$0.6 bar for the majority of the examples. This inferred basal shear stress value is almost 1/3 of the average basal shear stress calculated for the Greenland ice sheet. What causes this lower basal shear stress value on Mars is unclear but could involve the strain-weakening behavior of ice.

Citation: Banks, M. E., and J. D. Pelletier (2008), Forward modeling of ice topography on Mars to infer basal shear stress conditions, *J. Geophys. Res.*, *113*, E01001, doi:10.1029/2007JE002895.

1. Introduction

[2] The Martian polar regions have accumulated extensive mantles of ice and dust with volumes of $\sim 10^6$ km^3 [*Smith et al.*, 1999]. The layered deposits in these regions are believed to preserve a record of seasonal and climatic cycling of atmospheric carbon dioxide, water, and dust over the past hundred million to perhaps even billion years [*Pathare et al.*, 2005]. In addition to the polar caps, persuasive evidence of past glacial processes has been identified in areas such as the Argyre Basin, east of Hellas Basin, the northern fretted terrain, and among the Tharsis volcanoes [e.g., *Head*, 2000; *Head and Marchant*, 2003; *Head et al.*, 2005, 2006; *Moore and Davis*, 1987; *Kargel*, 2004; *Kargel and Strom*, 1990, 1992]. Understanding more about the history of ice on Mars could reveal important information about Martian geologic and climatic history including variations in insolation, orbital parameters, volatile mass balance, large impacts, volcanic eruptions, catastrophic floods, and solar luminosity. To learn more about the past and present ice of Mars and its climatic and geologic implications, a model is needed that operates over complex topography capable of both ice reconstruction and forward modeling of erosion and deposition.

[3] Previous approaches to the modeling of ice cap geometry and flow on Mars can be divided into simple ''flow band'' models that predict ice surface elevations along a one-dimensional (1-D) flow band in the x direction, and more sophisticated ''map plane'' models that predict surface elevations in the x and y directions. Models previously developed by *Schmidt and Buchardt* [2004], *Fountain et al.* [2000], *Moore and Davis* [1987], and *Hvidberg* [2002] have given valuable insight into possible mass balance processes, flow velocities, and the flow regime surrounding scarps and troughs of the Martian polar ice sheets. A wide range of information about the ice on Mars has also been provided by the more sophisticated models of *Fisher* [1993], and *Pathare et al.* [2005]. Particularly important is the dynamic/thermodynamic ice sheet model SICOPOLIS [e.g., *Greve*, 2000; *Greve et al.*, 2003, 2004; *Greve and Mahajan*, 2005; *Mahajan et al.*, 2004]. Generally speaking, flow band models are advantageous in that they are more readily calibrated and interpreted. They are well suited for first-order ice sheet modeling but are of limited usefulness when applied to complex or steep bed topographies. Map plane models are more versatile and accurate in principle but require input parameters that may be difficult to constrain. A model is needed that incorporates the physical realism of the map plane models and their ability to work

[1]Department of Geosciences, University of Arizona, Tucson, Arizona, USA.

0148-0227/08/2007JE002895

with complex bed topographies with the simplicity of flow band models. This becomes particularly important when reconstructing bodies on other planets, such as Mars, where parameter estimation may be far more challenging than on Earth.

[4] In this study, we developed a threshold-sliding model based on the work of *Nye* [1951, 1952a, 1952b] and *Reeh* [1982, 1984] that is designed to capture the realism of map plane models with complex topography while minimizing the number of required input parameters. *Nye*'s [1951] classic work on the geometry of perfectly plastic ice sheets and glaciers has long been used to estimate the thicknesses of former ice sheets. In his work, Nye developed a differential equation for the ice surface topography above an arbitrary or known bed if flow lines are known, which was later incorporated into the models of Reeh and colleagues [e.g., *Reeh*, 1982, 1984; *Fisher et al.*, 1985]. The Nye-Reeh model was found to be applicable to ice sheets and glaciers that move when a threshold shear stress has been exceeded and was successfully used to reconstruct the Antarctic ice sheet [*Reeh*, 1982, 1984]. However, this model utilized a complicated computational approach.

[5] In this paper we update the Nye-Reeh model with a new numerical algorithm. In this model, the geometry of present and past ice sheets and glaciers can be reconstructed using information about bed topography, ice margin positions, and threshold basal shear stresses. The advantage of this model, especially when applied to the surfaces of other planets, is that it requires constraints on only one physical parameter: the threshold basal shear stress. Research on Earth suggests that the value of the basal shear stress is constant on spatial scales of tens of kilometers and varies in a systematic way at larger spatial scales. While the threshold-sliding model works well in many cases, it has several well known limitations. For example, it cannot model the thermal effects on basal conditions nor can it represent surging and tidal forces when ice interacts with the ocean.

[6] We test the model by simulating the ice thickness and morphology of the Greenland ice sheet. By adjusting the model to the appropriate surface conditions on Mars, we also demonstrate its potential in reconstructing the ice surface topography of modern and former ice sheets and glaciers on other planets. We also constrain modern basal shear stresses and discuss the implications for bed environmental conditions on Mars. To do this, we use the threshold-sliding model to reconstruct ice that drapes impact craters near the margins of the south polar layered deposits (SPLD). This application was chosen because it enables us to make relatively accurate predictions about the ice margins and the bed topography underneath the ice due to the radial symmetry of impact craters. The threshold-sliding model also provides a basis for a glacial erosion model that can be used to better understand the spatial distribution of glacial erosion for areas such as the Argyre basin on Mars.

2. Model Description

2.1. Previous Work

[7] Field studies of modern ice sheets and glaciers on Earth have often shown that basal shear stress values lie between 0.5 and 1.5 bars [*Nye*, 1952a, 1952b], a surprisingly narrow range considering the spatial variability of observed basal conditions, including gradients in temperature, meltwater content, basal debris, till rheology, and other variables. *Nye* [1951, 1952b] developed a differential equation for the ice surface topography above an arbitrary or known bed if the flow lines are known, which was later incorporated into the models of *Reeh* and colleagues [e.g., *Reeh*, 1982, 1984; *Fisher et al.*, 1985]. While his equation yields parabolic and logarithmic solutions for flat and inclined beds, solutions for more complex bed topography can be obtained numerically. The Nye-Reeh model is not only associated with perfectly plastic deformation of near-basal ice but is also applicable to complex basal mechanisms such as debris controlled frictional sliding and till deformation [*Reeh*, 1982, 1984]. It can be used with any ice sheets and glaciers that move when a prescribed threshold shear stress is exceeded whether relative motion occurs internally or by sliding over deforming till or directly over the bed [*Reeh*, 1982, 1984]. Threshold behavior may characterize these basal processes under many conditions, including the plastic behavior of deforming till [e.g., *Tulaczyk et al.*, 2000] and the shear stress necessary to overcome kinetic friction during basal sliding [e.g., *Lliboutry*, 1979]. In this paper we use the term "threshold sliding" to refer to the class of ice sheets and glaciers that move when a threshold basal shear stress is exceeded.

[8] Critical to Nye's success in developing a single, independent equation for the geometry of ice sheets was his observation that the ice sheet geometry is independent of flow when the relative motion of the ice sheet and its bed is governed by a threshold shear stress. In these cases, the local ice thickness continually adjusts to the local ice surface slope to maintain a balance of forces independent of the pattern of accumulation and ablation. Accumulation and ablation rates affect the velocities of ice sheets and glaciers, but not their geometries as long as a threshold condition exists for motion and the margin is fixed or is a prescribed function of time. Used in conjunction with the Nye-Reeh model, information on the position of the ice margin enables the rates of accumulation and ablation to be eliminated from the reconstruction as long as the margin is static.

2.2. Basal Shear Stress

[9] The basal shear stresses in ice sheets and glaciers are given by [*Nye*, 1951]

$$\tau = \rho g h S \tag{1}$$

where ρ is the density of ice, g is the gravitational acceleration, h is the ice thickness, and S is the ice surface slope using a small angle approximation in which $\sin(S) = S$. Equation (1) assumes that gradients in longitudinal stresses are negligible, an accurate approximation for spatial scales several times the ice thickness [*Hooke*, 2005]. Field studies have long recognized that basal shear stresses calculated with equation (1) commonly range from about 0.5 to 1.5 bars [*Nye*, 1952a, 1952b]. *Nye* [1951] used this observation to invert equation (1) to solve for ice thickness. Expressed as a function of ice thickness, $h(x)$, and bed topography, $b(x)$, S is given by $S = |dh/dx + db/dx|$. Using

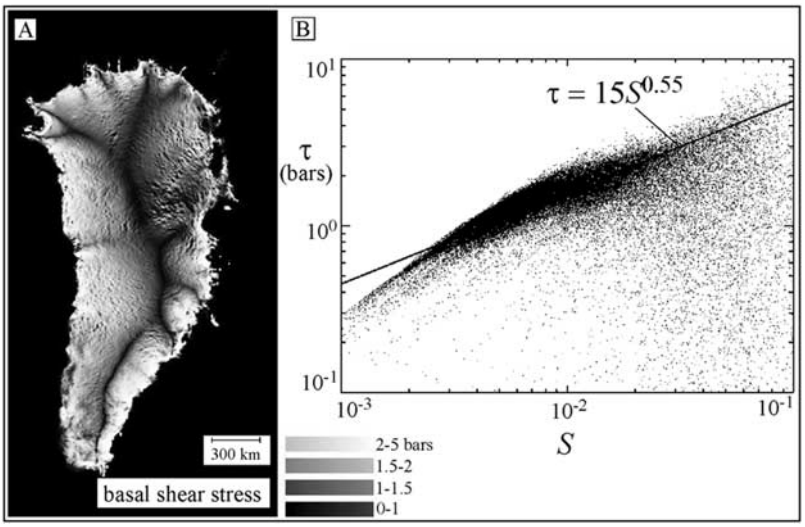

Figure 1. (a) Basal shear stresses beneath the Greenland ice sheet calculated from equation (1) and data sets of *Bamber et al.* [2001]. Legend gives brightness scale. Basal shear stresses vary from about 0.5 bar at divides to an average of 3 bars near margins. (b) Relationship of basal shear stress, τ, to ice surface slope. Each point represents a pixel from Figure 1a. A least squares power function fit to the data is indicated by the solid line.

this expression, equation (1) becomes a nonlinear differential equation for h:

$$\left|\frac{dh}{dx}+\frac{db}{dx}\right| = \frac{\tau}{\rho g h} \tag{2}$$

Equation (2) can be solved if τ and $b(x)$ are known and proper boundary conditions are applied. The boundary conditions for equation (2) are $h = 0$ at the two ice margins on either side of the divide.

[10] In addition to using a constant basal shear stress, the Nye-Reeh model can also be extended to include the spatial variability of basal shear stress observed in large modern ice sheets on Earth. Figure 1a is a gray scale image of the basal shear stresses in Greenland calculated from equation (1). This image clearly shows that basal shear stresses increase with distance from divides, with values ranging from 0.5 bar near divides to roughly 3 bars near margins, and have an average value of ~1.41 bars.

[11] One means of incorporating the observed spatial variability of basal shear stresses into the model is to consider them as a function of ice surface slope. In Figure 1b, the basal shear stresses of Greenland are plotted as a function of ice surface slope on a logarithmic scale. The plot illustrates that basal shear stresses increase from values as low as 0.5 bar at low slope values to higher, more variable values as slope values increase. A least squares power function fit to this data, ($\tau = 15S^{0.55}$), is indicated by the solid line in Figure 1b. Certainly a higher-order fit would characterize the data more precisely because the data set has a significant convex curvature in its dependence on ice surface slope. However, $\tau = 15S^{0.55}$ provides a useful first-order correction to uniform basal shear stresses. Quantifying basal shear stresses as a function of distance from divides was also investigated but did not provide as clear a correlation. Power function fits such as $\tau = 15S^{0.55}$, characterize most of the spatial variability in basal shear stress, but the limitations of the power function can be recognized in the reconstructions. In particular, divide regions in the model reconstructions have ice surface slopes that are noticeably steeper than in real ice sheets. However, these inaccuracies are limited to the divide region. Therefore, for large ice sheets, power function fits can be used as the basis for incorporating nonuniform basal shear stresses in the threshold-sliding model by replacing τ with $\tau(S)$ in equation (2).

2.3. Ice Sheet and Glacier Reconstructions in Three Dimensions

[12] In three dimensions, equation (2) applies along the direction of flow lines. Since flow lines are parallel to the local ice surface gradient, the 3-D version of equation (2) is obtained by replacing $S = |dh/dx + db/dx|$ with $S = |\nabla h + \nabla b|$ to obtain

$$|\nabla h + \nabla b| = \frac{\tau}{\rho g h} \tag{3}$$

The basal shear stress may also be written as a function of S, $\tau(S)$, to incorporate spatial variations as observed in Figure 1. As a solution to equation (3), we have developed a straightforward algorithm based on the accumulation of discrete ''blocks'' of ice on a grid. Our method mimics the accumulation of ice thickness and slope until a threshold is reached (illustrated schematically in Figure 2). Before the algorithm begins, grid points within the ice margin are identified. Ice will accumulate at these points while the other grid points remain ice free. The fundamental action item for each allowed grid point is simple: add a discrete unit of ice thickness if the resulting surface slope is less than a threshold value given by $\tau/\rho g h$. The ice surface slope is calculated as $S = (S_x^2 + S_y^2)^{1/2}$ where S_x is the downhill slope in the x direction and S_y is the downhill slope in the y direction. During each ''sweep'' of the grid, the algorithm

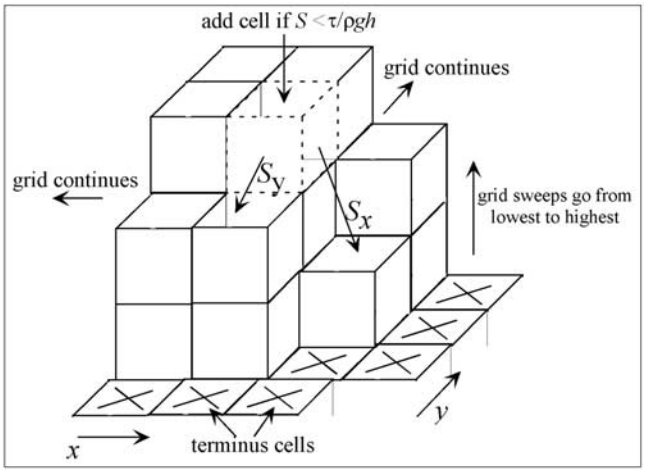

Figure 2. Illustration of our discrete algorithm method for solving equation (3). At each iteration of the algorithm, a unit of ice is added to each grid point within the area of ice coverage if the addition does not violate the condition that $S < \tau/\rho gh$ (where S is the ice surface slope equal to $(S_x^2 + S_y^2)^{1/2}$). The ordering of the grid points is important in this algorithm. In order to avoid oversteepenings, the sweep through the grid should be from lowest to highest elevations.

attempts to add ice to all of the allowed grid points. The grid is swept repeatedly until no additional blocks can be added. The end result is an exact solution to equation (3) for any bed topography. The value of τ can be taken to be uniform in this model or it can be a function of the ice surface slope. Each sweep through the grid is from lowest to highest elevations to avoid oversteepening and to make the model more efficient. A coarse block size is used initially and is reduced in size by a constant factor once no more blocks can be added to the grid. This enables a coarse solution to be obtained quickly which is gradually smoothed as the block size is reduced. It should be emphasized that although this algorithm method is discrete, it is not a cellular automaton or otherwise an approximation to equation (3). Instead, it is an iterative numerical method that obtains an exact solution to equation (3).

[13] It should be noted that there are different methods that have been applied to ice sheet modeling. Traditionally, ice sheet modeling has been based on prescribing climatic factors, such as the spatial distribution of net accumulation rate, over the potential ice-covered area and letting the ice sheet build up both vertically and laterally with free margins. This method utilizes inputs for climate or net accumulation together with ice rheology/threshold basal shear stress to model the ice sheet forward in time from some specified starting condition. However, if the ice margins are known, the ice sheet topography can also be reconstructed by starting the reconstruction method with the full lateral extent of the ice and growing the cap vertically until the threshold basal shear stress is reached. In this approach, only the ice margin and the threshold basal shear stress are needed as inputs. It is important to emphasize that this alternative method is static and does not reconstruct any of the intermediate stages in ice sheet growth. Instead, the algorithm only reconstructs the ice sheet topography for the "snapshot" of time at which the ice sheet occupies that specific margin. In this study we utilized this method because the spatial pattern of mass balance or net accumulation on Mars is unknown. A set of climatic conditions does exist that created the resulting ice morphology seen today. However, since these conditions are unknown, we use this method as a way to obtain the same end result. The efficiency of the model is demonstrated by comparing the reconstructed ice surface topographies with those observed. Of course, the threshold-sliding model can also be run using a spatial mass balance distribution instead of an ice terminus for instances in which the ice margin at a given time is unknown. When run this way, the model moves the ice sheet both upward and outward with the ice margin free to take on any shape in response to spatial variations in net accumulation and threshold basal shear stress.

3. Validation of the Threshold-Sliding Model to the Modern Greenland Ice Sheet

[14] In this section we present a reconstruction of the ice surface topography of the modern Greenland ice sheet using our discrete algorithm method as a solution to equation (3). Greenland is an important case study because the bed topography is both well constrained and has a significant influence on the morphology of the ice sheet. Specifically, the principal divide in Greenland is offset from central Greenland by approximately 100 km (a flat bed would place the divide in the middle). This asymmetric profile could reflect a bed topographic control associated with higher bed elevations in eastern Greenland. Alternatively, the asymmetry of the ice sheet may be associated with an east-to-west accumulation gradient similar to that observed today [*McConnell et al.*, 2000].

[15] Figures 3a and 3b illustrate the bed and ice surface topography for modern Greenland [*Bamber et al.*, 2001]. Areas below sea level are indicated in black (Figure 3a). This and all other reconstructions in the paper require three inputs: a DEM of bed topography, a "mask" grid defining the ice margin, and a function defining the basal shear stress. The bed topography was input directly into the model and the ice thickness data, derived from the difference between the ice surface and bed topography, was used to provide a binary "mask" grid defining the grid points that are allowed to accumulate ice. The mask grid has values of 1 where the ice thickness is greater than 0 (i.e., areas covered by ice), and values of 0 where the thickness is 0 (i.e., no ice coverage). For this reconstruction we used the shear stress relationship $\tau = 15S^{0.55}$ observed in Figure 1.

[16] Figure 3c is a shaded relief and contour map of the solution to equation (3) obtained by our discrete algorithm method. The shaded relief image has been constructed with the same vertical exaggeration (30x) as Figure 3b to provide a direct, side-by-side comparison. The similarity of the location and shape of the contours indicate that the overall solution is in good agreement with the observed topography. The location of the major divide, offset from center by approximately 100 km, is also reproduced in the model indicating that the asymmetry of the ice sheet is primarily the result of bed topographic control. One major difference between the observed and modeled topography, however, is

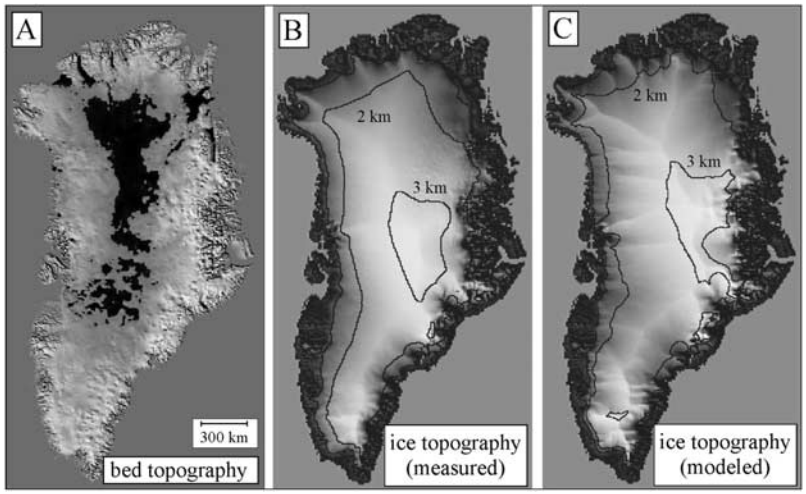

Figure 3. Reconstruction of the modern Greenland ice sheet using equation (3), and the observed correlation $\tau = 15S^{0.55}$ from Figure 1. Bed and ice surface topography are illustrated with shaded relief (30X vertical exaggeration) gray scale maps. (a) Input bed topography from *Bamber et al.* [2001]. Darkest areas are below sea level. (b) Ice topography observed from radar interferometry and given by *Bamber et al.* [2001]. Contours are 1 km in spacing (1 km contour is too close to the margin to be easily seen). (c) Numerical reconstruction of the ice surface topography (with the same gray scale and shading as in Figure 3b). The divide position and elevations are a good match to Figure 3b except that the divides are too peaked.

the steepness of divides and the more angular appearance of the modeled topography. This angularity can be traced to the poor fit between the power function and the data of Figure 1a. In the lower left corner of Figure 1b, representing areas of low slope, the data fall far below the power function indicating that the threshold basal shear stress near divides is significantly lower than the values predicted by the power function. As a result, the model solution overestimates the ice surface slopes near divides by as much as a factor of 2. However, this does not introduce significant errors in the elevations of these regions because the slopes in either case are small.

4. Application of the Model to Mars

4.1. Methods

[17] The model's ability to accurately reproduce ice sheets such as the one in Greenland is the basis for further testing of the model on Mars. To do this, we selected 10 partially ice covered impact craters in which ice has overtopped the crater rim. Craters were specifically chosen in which relatively accurate predictions of the bed topography underneath the ice could be made and in which the ice margins could be clearly determined. All of the craters are located near or on the edges of the SPLD which are composed of ice and dust [e.g., *Mellon*, 1996; *Durham et al.*, 1999; *Nye*, 2000; *Nye et al.*, 2000]. The locations of each crater are indicated with black boxes in Figure 4.

[18] As in the Greenland ice sheet example, reconstructions of ice thickness and morphology with the threshold-sliding model require three inputs: a DEM of bed topography, a "mask" grid defining the ice margin, and a function defining the basal shear stress. The bed topographies for the model could be determined due to the radial symmetry typical of impact craters. Craters were specifically chosen in which ice could clearly be seen to cover part but not all of the crater floor. Unless there has been significant subglacial erosion, the symmetry of the exposed crater form can be used to predict the morphology of the crater floor obscured beneath the ice. The software RiverTools [*RIVIX*, 2005] was used to extract multiple profiles through each crater from digital elevation models (DEMs) of the south polar cap and surrounding SPLD based on altimetry data acquired by the Mars Global Surveyor Mars Orbiter Laser Altimeter (MOLA) Instrument (data available at http://www.pds_geosciences.wustl.edu/missions/data). Each profile started at the center of the crater and was extended out past the crater rim along surfaces not obscured by ice. A custom computer program was then used to average the extracted profiles and create 3-D bed topography assuming radial symmetry.

[19] The margins of the ice were identified from the DEM based on changes in elevation and differences in surface texture. Profiles were extracted along the floors of the craters to determine the locations of sudden increases in elevation indicating the edge of the ice. Ice margins were also identified where the texture changed from the rough crater floor to the relatively smooth and layered appearance of the ice. These observations were later confirmed with higher resolution MOC and THEMIS images. The ice margins were converted into a binary "mask" grid defining the grid points allowed to accumulate ice as was done when applying the model to the Greenland ice sheet.

[20] For the basal shear stress, we investigated the effect of both constant basal shear stress and the spatial variability of basal shear stress, $\tau(S)$, on model simulations for each crater. Gravity was changed to match the gravity on Mars and ice density was given a value of 0.92 g/cm^3 based on the assumption that the ice in the SPLD is primarily H_20 ice [e.g., *Pathare et al.*, 2005; *Koutnik et al.*, 2005] and has the same physical properties as H_20 ice on earth [*Greve et al.*,

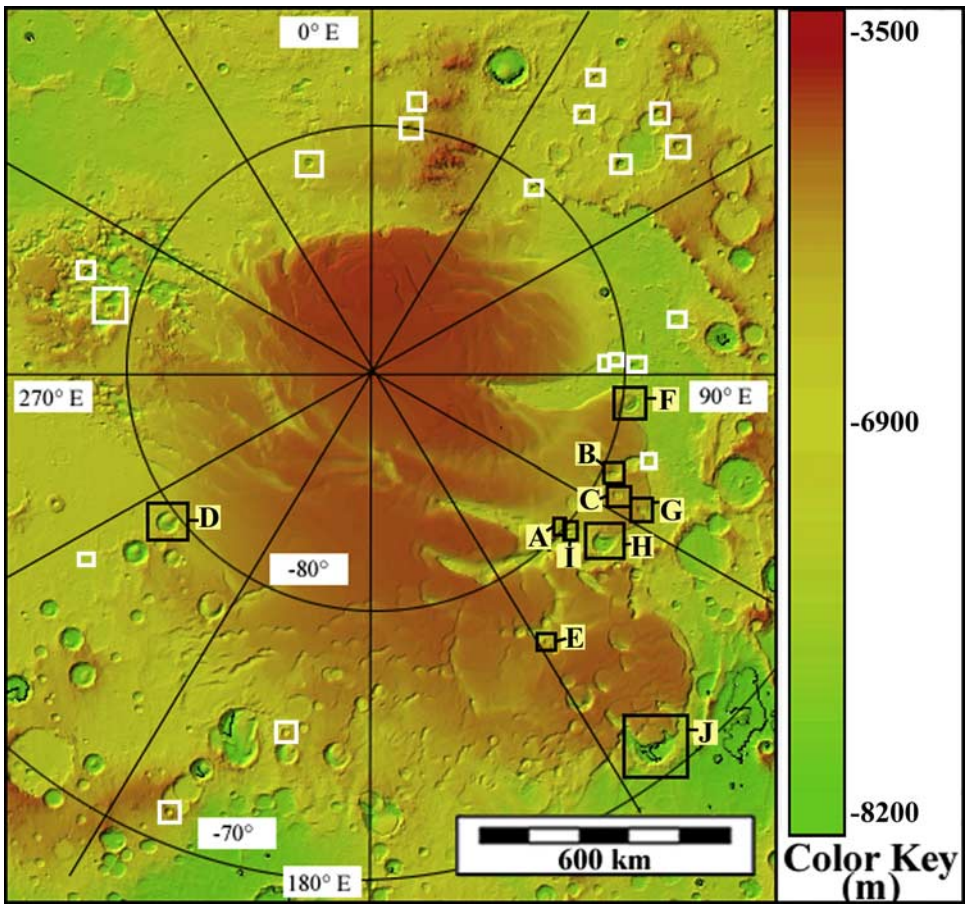

Figure 4. A shaded relief map of the south polar layered deposits. Ice-filled impact craters analyzed in this study are indicated with black boxes and labeled A–J. White boxes indicate the locations of impact craters measured for their central peak dimensions.

2003]. Forward modeling was then used to construct families of ice lobes corresponding to a series of basal shear stress conditions.

[21] Once completed, the elevation of the ice in each pixel of the model reconstructions was subtracted from the elevation of the ice in the corresponding pixel of the original DEM to determine an average ice elevation difference per pixel. This was done for the ice-covered areas within the crater only and excluded the surrounding ice-covered terrain where bed topography was not well constrained. This method enabled us to quantitatively determine which values of basal shear stress most accurately reconstructed the ice thickness and to establish the uniqueness of the results. Figure 5 shows plots for two impact craters of the average ice elevation difference per pixel (in meters) for a series of basal shear stresses. As can be seen in Figure 5, similar ice thicknesses are produced for a basal shear stress range of roughly ±0.1 bar. Model results were also analyzed visually to determine which values of basal shear stress best reconstructed the original ice morphology.

4.2. Determining the Bed Topography for Craters More Than Half Covered With Ice

[22] In determining the bed topographies for our model reconstructions, we encountered two different scenarios: crater floors that were less than half covered by ice and crater floors that were half or more than half covered with ice. For craters less than half covered with ice, the symmetry of the observed crater form could easily be used to estimate the morphology of the crater floor buried beneath the ice lobe as was already described. However, about half of the craters in our study were more than half covered with ice. In these cases, topographic information could be obtained from the rim to the base of the crater but information regarding any features potentially existing in the center of the crater floor was obscured by ice. To resolve this, it was necessary to investigate the characteristic dimensions of impact structures in the south polar region of Mars.

[23] Impact craters can be divided into different categories with different profiles and features. Two main categories are simple craters and complex craters. Simple craters have relatively smooth, bowl-shaped cross sections with upraised rims while complex craters are characterized by one or more central mountains (central peak) surrounded by a relatively flat floor inside of a terraced rim. As complex craters increase in size, other features, such as peak rings, may appear [e.g., *Baldwin*, 1949; *Pike*, 1988; *Melosh*, 1989]. Whether or not a simple or complex crater is formed by an impactor depends on factors such as the size of the impactor and the gravity of the planet it is impacting [e.g., *Barlow and Bradley*, 1990]. For Mars, the transition from a

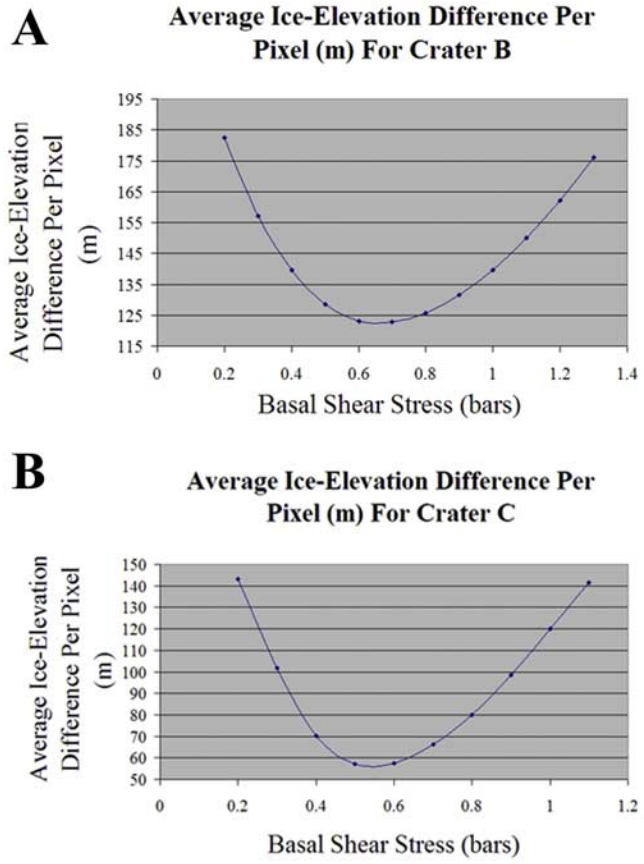

Figure 5. Average ice-elevation difference per pixel (in meters) from model reconstructions for (a) crater B and (b) crater C. This average difference per pixel was found by subtracting the elevation of the ice in each model reconstruction from the elevation of the ice in the original DEM. The subtraction was completed only for the ice-covered areas within the crater, not the ice-covered surrounding terrain where bed topography was not well constrained.

simple to a complex crater typically occurs at diameters of roughly 6 to 7 km [e.g., *Garvin et al.*, 2003]. In this study we look at impact craters on Mars within the diameter range of ~10–90 km and are therefore only concerned with complex crater morphologies that may or may not contain a central peak. The dimensions of central peaks, such as the basal diameter of the central peak (D_{cp}), and height of the central peak above the observed depth of the crater (h_{cp}), typically form in predictable ratios to the diameter (D) of the crater as measured from its rim crests (Figure 6a). The accepted relationships for these features on Mars as a whole are

$$D_{cp} = 0.25D^{1.05} \quad (4)$$

$$h_{cp} = 0.04D^{0.51} \quad (5)$$

where all distances are in kilometers [*Garvin et al.*, 2003]. These ratios, however, may change depending on factors such as the velocity of the impactor, the composition of the impacted surface, or the presence of subsurface volatiles [e.g., *Barlow and Bradley*, 1990; *Melosh*, 1989, *Cordell et al.*, 1974; *Cintala et al.*, 1976; *Hale and Head*, 1981].

[24] In order to make accurate predictions as to the bed topography under the ice in the central part of the craters, central peaks were measured and compared for multiple complex craters in the area surrounding the SPLD. The

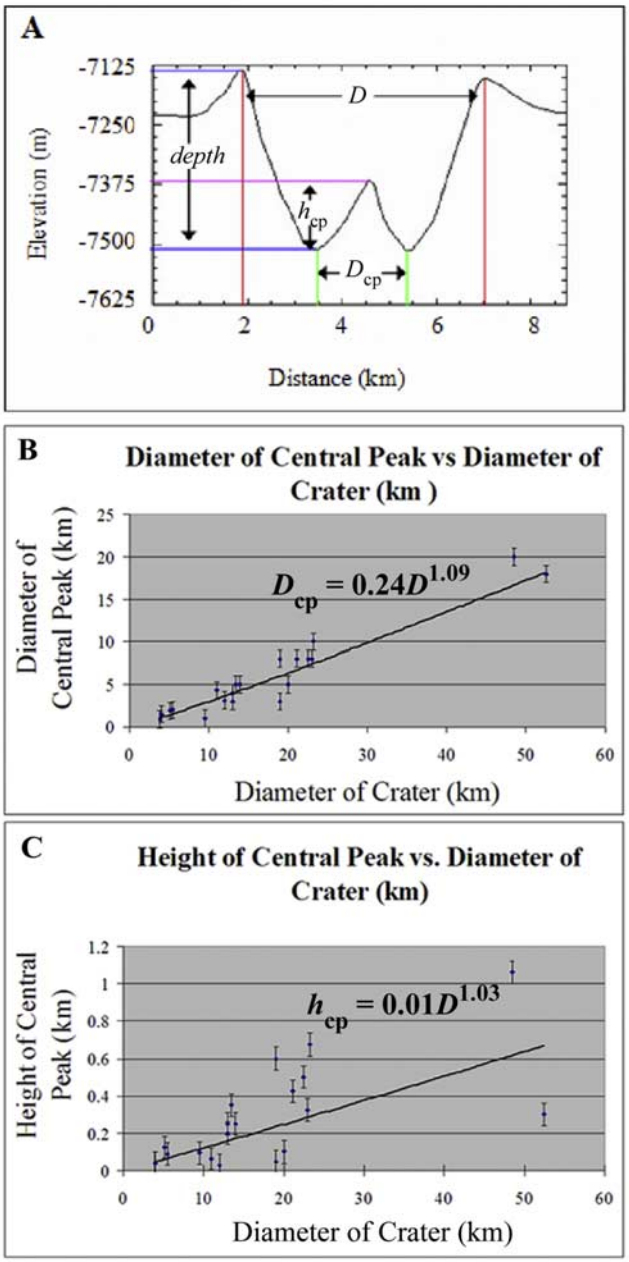

Figure 6. (a) Profile of a representative complex crater measured in this study. Labeled dimensions are D, diameter of crater between the rim crests; depth, observed depth of the crater; D_{cp}, basal diameter of the central peak; and h_{cp}, height of the central peak above the observed depth. (b) Diameter of central peaks plotted against crater diameters. (c) Height of central peaks plotted against crater diameters. For both Figures 6b and 6c, least squares power function fits are indicated by the solid lines.

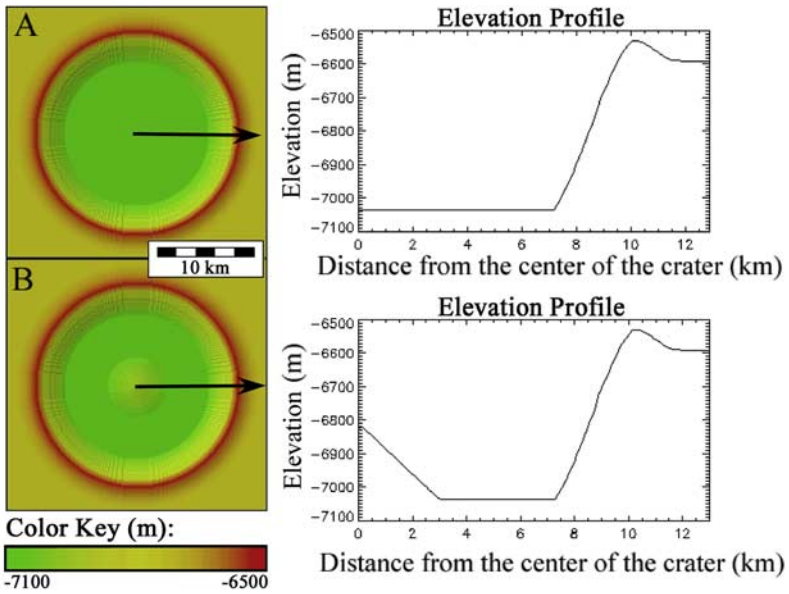

Figure 7. Shaded relief images and profiles of 3-D averaged bed topographies for crater G. (a) Flat crater floor. (b) Crater floor with a central peak. The black arrows indicate the location of the profiles and the direction in which they were drawn.

locations of these craters are indicated with white boxes in Figure 4 and the results are shown in Figures 6b and 6c where D is plotted against D_{cp} and h_{cp}, respectively. Least squares power function fits are marked by the solid lines in the plots (Figures 6b and 6c) and indicate the following relationships:

$$D_{cp} = 0.24D^{1.09} \tag{6}$$

$$h_{cp} = 0.01D^{1.03} \tag{7}$$

where all distances are in kilometers. The difference between the *Garvin et al.* [2003] relationship and our measured relationship of D_{cp} to D is insignificant. Therefore, for determining the diameter of potential central peaks beneath the ice, we used the *Garvin et al.* [2003] equation (4). Our measured relationship of h_{cp} to D indicates that in comparison to nonpolar craters on Mars, craters in the area surrounding the SPLD have central peaks that are lower in elevation for smaller craters ($D < \sim 15$ km) and higher in elevation for larger craters. The reasons for this are beyond the scope of this paper but may include the presence of subsurface volatiles, viscous creep relaxation, and/or infilling or erosional processes in the polar regions [e.g., *Garvin et al.*, 2000; *Thomas et al.*, 1992; *Pathare et al.*, 2005; *Schaller et al.*, 2005]. Therefore, to determine the height of potential central peaks beneath the ice, equation (7) was used.

[25] To simulate a crater with a flat floor (no central peak), the lowest elevation point on each profile was extended across the length of the crater floor. To simulate a crater floor with a central peak, the lowest elevation point on each profile was again extended and equations (4) and (7) were used to create a central cone structure of the appropriate dimensions simulating the approximate shape and elevation of a central peak. A custom computer program was then used to separately average both sets of profiles and create two different 3-D bed topographies for each crater; one representing a flat crater floor and one representing a central peak at the center of the crater floor (Figures 7a and 7b).

4.3. Results

[26] The majority of the model results indicated a constant basal shear stress range of 0.5–0.7 bar (craters A through E). Several outliers also indicated constant basal shear stress ranges of 1.1–1.4 bars (craters F and G) and 1.9–2.4 bars (craters H, I, and J). With the exception of craters H, I, and J, the use of constant basal shear stress, τ, with the model produced better matching ice morphologies than did a slope-dependent shear stress, $\tau(S)$. Therefore we will refer to our results in terms of constant basal shear stress unless otherwise indicated. Results are summarized in Table 1 and Figures 8 and 9 show shaded relief images for each crater and our most accurate model simulation followed by the best matching profiles for comparison of ice thickness and morphology. The location and direction of each profile is indicated by the black arrows in each crater. Elevation data is in relation to the zero datum elevation on Mars and has an offset of −8000 m.

[27] The ice thickness in the majority of the craters (craters A–E) was best reconstructed using a constant basal shear stress of ∼0.6 bar (Figure 8). In general, the ice thickness, particularly near the rims of the craters, and the ice geometry are well reconstructed by the model. For crater D, even the small bump at the ice margin has been simulated. In a few instances however, (craters A and E), the ice surface slope near the margins tapers either too gradually or too steeply in the model simulations.

Table 1. Summary of Model Results

Crater	Latitude	Longitude	Diameter (Between Rim Crests), km	Inferred Basal Shear Stress, bars	Central Peak Included in Bed Topography	Uncertainties	Notes
A	−80.5°	130°E	9	0.5	na	none	ice thickness matches well near the rim of the crater but the ice tapers too gradually toward the ice margin in the simulation
B	−80°	113°E	28	0.7	na	some ice may be incorporated into the bed topography; ice margin slightly unclear	ice thickness and surface slope match very well
C	−79.5°	117°E	23	0.5	yes	position of the central peak	average ice thickness, surface slope, and morphology match well near the ice margin
D	−79.5°	235°E	53	0.7	no	ice margins unclear; lowest depth may be obscured	average ice thickness matches well; note that the small bump at the ice margin has been simulated by the model
E	−77.5°	149°E	14	0.5	yes	ice margins unclear; lowest depth may be obscured	ice thickness and surface slope match very well; the edge of the ice in the simulation ends with a slightly steeper slope
F	−80°	97°E	40	1.1	no	ice margins unclear; lowest depth may be obscured	ice thickness matches well but the surface slopes differ slightly
G	−78.5°	117°E	20	1.4	no	ice margins unclear	ice thickness and surface slope match almost perfectly near the crater rim
H Katoomba Crater	−79°	127°E	50	2.2 ($\tau = 9S^{0.55}$)	na	some ice may be incorporated into the bed topography; asymmetrical shape of crater is simulated as symmetrical	average ice thickness matches well but the ice tapers more gradually near the ice margin in the simulation; ice morphology matches slightly better when using a slope-dependent shear stress
I	−80.3°	130°E	13	2.4 ($\tau = 7S^{0.55}$)	na	none	average ice thickness, surface slope, and morphology match very well; ice morphology matches slightly better when using a slope-dependent shear stress
J	−72°	144° E	90	1.9 ($\tau = 11S^{0.55}$)	na	some ice and dunes are incorporated into the bed topography	average ice thickness matches well but the surface slopes differ; ice morphology matches slightly better when using a slope-dependent shear stress

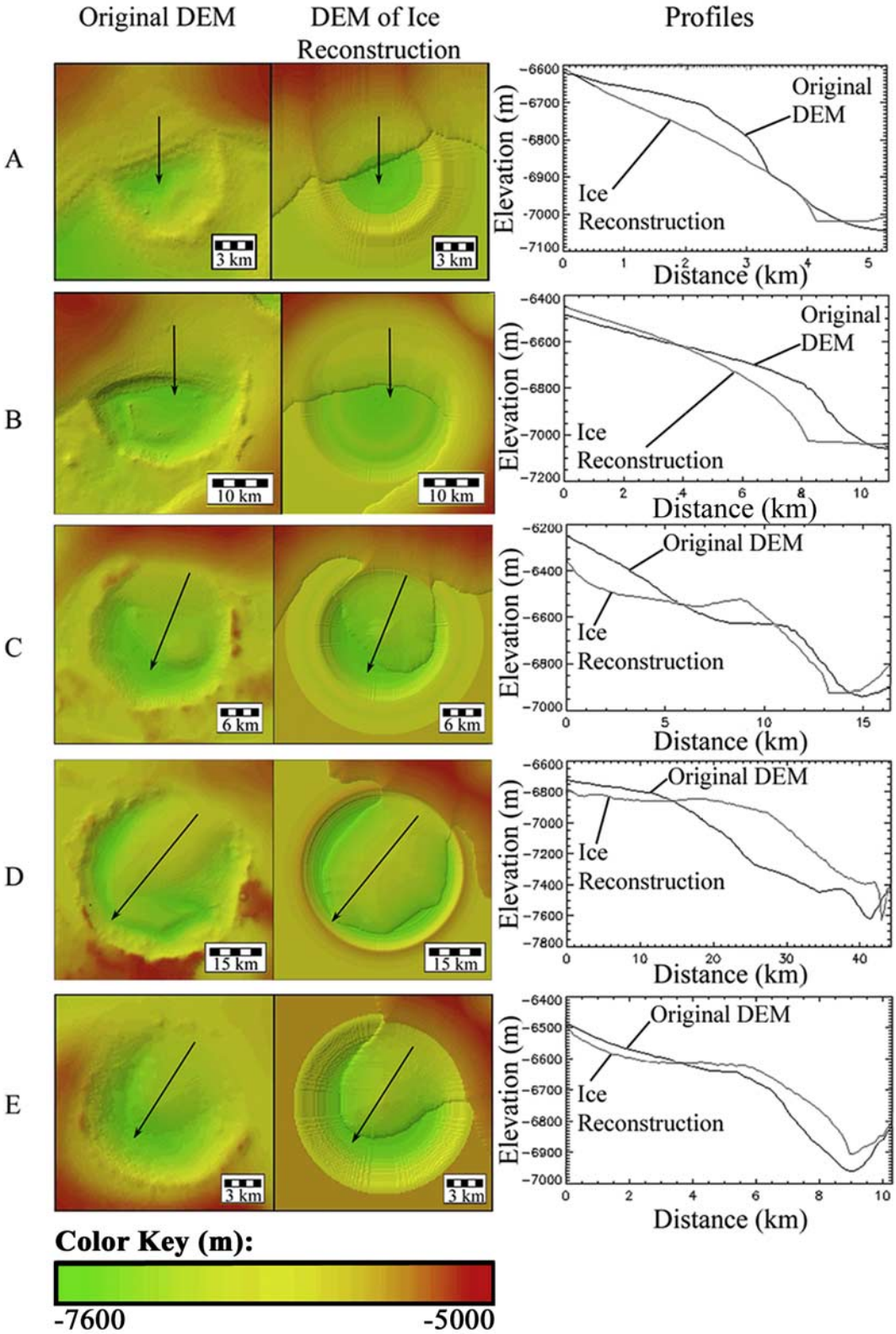

Figure 8. Shaded relief images and profiles for craters A–E and model simulations using a constant basal shear stress of ~0.6 bar. The black arrows indicate the location of the profiles and the direction in which they were drawn.

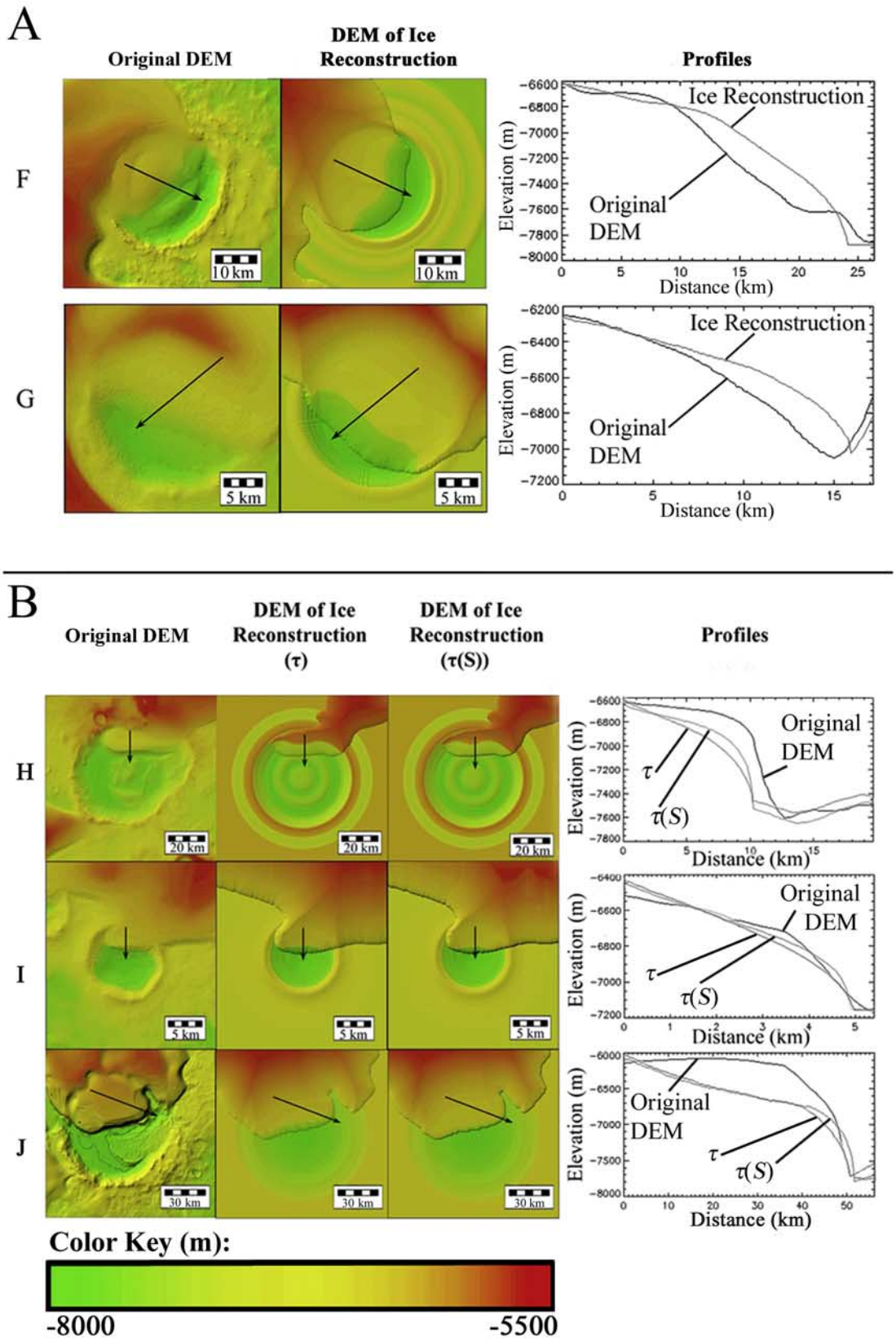
A
Original DEM
DEM of Ice Reconstruction
Profiles
F
G
10 km
5 km
Ice Reconstruction
Original DEM
Elevation (m)
Distance (km)
B
Original DEM
DEM of Ice Reconstruction (τ)
DEM of Ice Reconstruction (τ(S))
Profiles
H
I
J
20 km
5 km
30 km
τ
τ(S)
Color Key (m):
-8000
-5500

Figure 9

[28] A threshold basal shear stress of ~1.25 bars was used to model craters F and G (Figure 9a). For both of these craters, the ice thickness, particularly near the crater rim, matches very well. A constant threshold basal shear stress of ~2.15 bars was used for the reconstructions of ice morphology for craters H, I, and J (Figure 9b). In the profiles it can be seen that the ice thickness was generally well simulated. However, the actual ice surface slopes are relatively flat with steep slopes at the margin creating a blunt edge while, in the simulations, the ice tapers more gradually and consistently to the ice margin. The reasons for the ice surface slopes in craters H, I, and J are unclear. When comparing the dimensions of these three craters to those of the other craters in this study, their flat and blunt ice surface slopes were not found to be related to crater diameter, depth, or the slopes of the crater rims. However, the ice morphology was best simulated when spatial variations in basal shear stress were taken into account. This was done by using the shear stress relationships $\tau = 9S^{0.55}$, $\tau = 7S^{0.55}$, and $\tau = 11S^{0.55}$ for craters H, I, and J, respectively (Figure 9b). In comparison to the model simulations using a constant basal shear stress, the use of a slope-dependent shear stress maintained the same average ice thickness but created slightly more blunt edges near the ice margins.

[29] On the basis of the model results, the crater rims in the bed topography under the ice are too pronounced. Most likely, the actual crater rims under the ice have been altered or eroded more extensively than the parts of the rims that can be observed directly. Since we did not have a method for accurately estimating the subglacial erosion, the exposed parts of the rim were averaged for each crater and used as the entire rim in the bed topography. The profiles in Figures 8 and 9 were therefore drawn starting just inside the rims and extended toward the center of the crater roughly perpendicular to the ice margin to show only the areas of ice coverage for which a well constrained bed topography was used. Quantitatively, the presence or absence of a central peak beneath the ice did not change the value of basal shear stress inferred from the simulation that best reconstructed the ice thickness. However, in a few instances (craters C, E, and F), the presence of a central peak in the bed topography produced the best matching morphology.

[30] In summary, the threshold-sliding model was successful at creating accurate reconstructions for both the Martian examples and the Greenland ice sheet. Overall, a constant shear stress proved more accurate than a slope-dependent shear stress for the Martian simulations. However, this may be due to the smaller spatial scales of these reconstructions (i.e., tens, not hundreds of kilometers). Data from the Mars Advanced Radar for Subsurface and Ionospheric Sounding (MARSIS) on the Mars Express orbiter should provide information about the bed topography beneath both Martian polar caps. Once this information becomes available, the threshold-sliding model can be calibrated with the larger spatial scale of the Martian polar caps to determine whether τ or $\tau(S)$ is more appropriate when using the model to reconstruct the thickness and morphology of large expanses of ice on Mars.

5. Discussion

[31] The basal shear stresses inferred from the model reconstructions represent the basal shear stress values at which a threshold is reached. Any additional stress will cause some type of deformation or movement of the ice. The threshold-sliding model is able to account for basal sliding of the ice with no internal deformation, internal deformation of the ice with no basal sliding, or a combination of both, but it does not give any information about which of these processes is taking place. Although our results showed a range of values, the majority of the reconstructions in this study indicated an average threshold basal shear stress of ~0.6 bar or almost 1/3 that found for the Greenland ice sheet (~1.41 bars) on Earth. The causes behind the overall lower shear stresses associated with ice on Mars are unclear and factors that influence the yield strength of the ice and/or the coefficient of friction at the base of the ice should be investigated.

[32] One possible explanation for the low basal shear stresses on Mars is a reduced yield strength of the ice. On Earth, it has been found that the crystal sizes of ice vary directly with temperature and indirectly with strain rates. Potentially, lower temperatures, such as those found on Mars, can cause ice to form smaller crystal sizes which in turn could cause a lowering of the yield strength and thus an increase in the internal deformation rate [*Hooke*, 2005]. In addition, the orientation of ice crystals has been found to have a significant effect on shear strain rates [*Hooke*, 2005; *Li et al.*, 1996] and impurities, such as dust, salt, clathrates, or a proportion of carbon dioxide ice mixed in with the water ice, can cause softening or stiffening of the ice thus influencing the yield strength [e.g., *Greve and Mahajan*, 2005, *Greve et al.*, 2004].

[33] Other possible explanations for the low basal shear stresses found in our study could involve a lower coefficient of friction at the base of the ice which would lead to an increase in basal sliding. For example, producing meltwater at the base of a glacier increases the water pressure and results in a reduction in resistive drag at the bed and a decrease in the viscosity of the ice [*Hooke*, 2005]. Causes of basal melting could include climate changes, obliquity changes, frictional melting due to cap movement, or melting due to pressure from the overlying ice cap [*Fishbaugh and Head*, 2002; *Greve et al.*, 2004]. Basal melting could also result from modification of the melting point due to impurities in the ice or warmer temperatures at the base of the ice resulting from reduced heat conductivity [*Greve and Mahajan*, 2005; *Greve et al.*, 2004; *Fishbaugh and Head*, 2002] or a temporary heat source under the ice such as a volcanic eruption or a tectonothermal event [*Greve et al.*, 2004; *Fishbaugh and Head*, 2002]. However, in simulations conducted by thermodynamic models, basal temperatures were consistently found to be far below pressure melting

Figure 9. (a) Shaded relief images and profiles for craters F and G and model simulations using a constant basal shear stress of ~1.25 bars. (b) Shaded relief images and profiles for craters H, I, and J and model simulations using a constant basal shear stress (τ = ~2.15 bars) and slope-dependent shear stresses ($\tau(S)$). The black arrows indicate the location of the profiles and the direction in which they were drawn.

[*Greve et al.*, 2004]. Although melting may not occur, basal temperatures could still be a principal parameter affecting ice rheology and the rate of ice flow as simulations have shown that higher temperatures, although still below pressure melting, can produce higher rates of flow [*Paterson*, 1994; *Greve et al.*, 2004].

[34] The majority of the model results indicated a constant basal shear stress of ~0.6 bar which is consistent with the calculated values of ~0.5 bar for areas near the divides in the Greenland ice sheet (Figures 1a and 8). Several simulations also indicated basal shear stress values of ~1.25 and ~2.15 bars which are similar to values found closer to the margins of the Greenland ice sheet (Figures 1a and 9). Potentially, these three values could be reflecting different basal conditions on Mars that are comparable to the different basal conditions existing between the divides and the margins of the Greenland ice sheet. When investigating the bed topography for each of the craters, no significant differences in the ratio of crater depth to crater diameter or surface slope could be found. *Zwally and Saba* [1999] calculated basal shear stresses for the Martian north polar cap from observed surface slope and gravitational forcing and also found three distributions of shear stress, although these values were lower than those found in this study. Even though the average threshold basal shear stress values for the Earth and Mars examples in this study differ by ~1/3, the total range in values found for Mars, 0.5–2.4 bars, is consistent with the range of values calculated for the Greenland ice sheet, 0.5–3 bars (Figure 1a), and all but three of the Martian simulations inferred values that fall within the range of 0.5 to 1.5 bars reported by *Nye* [1952a, 1952b]. When reconstructing former ice sheets and glaciers on Mars (using modern conditions), families of reconstructions should be investigated for this full range of threshold basal shear stresses. When reconstructing large expanses of ice, the spatial variability in basal shear stresses, $\tau(S)$, as well as constant basal shear stresses, τ, should be investigated.

[35] A possible source of error in our results could be caused by the depths used for the crater bed topography. The averaged bed topography used as input for the model was based on current crater depths. Since we do not know exactly when the craters became covered with ice, possible alterations to the crater depth and morphology since the time of ice coverage have not been taken into account. Most likely these alterations would be small and would not significantly influence our results as was the case with the addition of a central peak to the bed topography of craters more than half covered with ice.

[36] Another limitation of the model in reconstructing past ice sheets on Mars is that the results of this study infer rheological conditions of modern ice which may be different from past ice. However, these experiments provide a starting point for model parameter estimation. For future work, knowledge of the temperature dependence of glacial flow parameters on Earth will allow us to increase or decrease the inferred modern values corresponding to a range of climatic conditions.

6. Summary

[37] Using the threshold-sliding model, we reconstructed the thickness and morphology of the Greenland ice sheet and ice draping the rims and partially filling impact craters on the margins of the layered deposits in the south polar region of Mars. An equation for shear stress as a function of surface slope, $\tau = 15S^{0.55}$, was used when reconstructing the thickness of the Greenland ice sheet while a constant basal shear stress of ~0.6 bar was used for the majority of the Mars examples. The ice thicknesses of several outliers in the Martian examples were also reconstructed using constant shear stress values of ~1.25 and ~2.15 bars. When reconstructing former ice sheets and glaciers on Mars (using modern conditions), families of reconstructions should be investigated for this full range of constant threshold basal shear stresses. When reconstructing large expanses of ice, the spatial variability in basal shear stresses should also be investigated. The reasons for the lower values of basal shear stress found for the Mars examples are unclear but could involve higher rates of internal deformation and/or increased rates of basal sliding.

[38] **Acknowledgments.** This research is supported by the NASA Mars Fundamental Research Program, grant NNG05GM30G.

References

Baldwin, R. B. (1949), *The Face of the Moon*, Univ. of Chicago Press, Chicago, Ill.

Bamber, J. L., L. P. Layberry, and S. P. Gogenini (2001), A new ice thickness and bedrock dataset for the Greenland ice sheet: 1. Measurement, data reduction, and errors, *J. Geophys. Res.*, *106*(D24), 3177–3180.

Barlow, N. G., and T. L. Bradley (1990), Martian impact craters: Correlations of ejecta and interior morphologies with diameter, latitude, and terrain, *Icarus*, *87*, 156–179.

Cintala, M. J., J. W. Head, and T. A. Mutch (1976), Martian Crater depth/diameter relationships: Comparison with the Moon and Mercury, *Proc. Lunar Sci. Conf. 7th*, 3575–3587.

Cordell, B. M., R. E. Lingenfelter, and G. Schubert (1974), Martian cratering and central peak statistics: Mariner 9 results, *Icarus*, *21*, 448–456.

Durham, W. B., S. H. Kirby, and L. A. Stern (1999), The rheology of solid carbon dioxide: New measurements, *Lunar Planet. Sci. Conf.* [CD-ROM], *XXX*, Abstract 2017.

Fishbaugh, K. E., and J. W. Head III (2002), Chasma Boreale, Mars: Topographic characterization from Mars Orbiter Laser Altimeter data and implications for mechanisms of formation, *J. Geophys. Res.*, *107*(E3), 5013, doi:10.1029/2000JE001351.

Fisher, D. A. (1993), If Martian ice caps flow: Ablation mechanisms and appearance, *Icarus*, *105*, 501–511.

Fisher, D. A., N. Reeh, and H. B. Clausen (1985), Stratigraphic noise in the time series derived from ice cores, *Ann. Glaciol.*, *7*, 76–83.

Fountain, A., J. Kargel, K. Lewis, D. MacAyeal, T. Pfeffer, and J. Zwally (2000), Troughs on Martian ice sheets: Analysis of their closure and mass balance, paper presented at International Conference on Mars Polar Science and Exploration, Lunar and Planet. Sci., Reykjavik.

Garvin, J. B., S. E. H. Sakimoto, J. J. Frawley, and C. Schnetzler (2000), North polar region craterforms on Mars: geometric characteristics from the Mars Orbiter Laser Altimeter, *Icarus*, *144*, 329–352.

Garvin, J. B., S. E. H. Sakimoto, and J. J. Frawley (2003), Craters on Mars: global geometric properties from gridded MOLA topography, paper presented at Sixth International Conference on Mars, Calif. Inst. of Technol., Pasadena, Calif.

Greve, R. (2000), Waxing and waning of the perennial north polar H_2O ice cap of Mars over obliquity cycles, *Icarus*, *144*, 419–431.

Greve, R., and R. A. Mahajan (2005), Influence of ice rheology and dust content on the dynamics of the north-polar cap of Mars, *Icarus*, *174*, 475–485.

Greve, R., V. Klemann, and D. Wolf (2003), Ice flow and isostasy of the north polar cap of Mars, *Space Sci.*, *51*, 193–204.

Greve, R., R. A. Mahajan, J. Segschneider, and B. Grieger (2004), Evolution of the north-polar cap of Mars: A modelling study, *Planet. Space Sci.*, *52*, 775–787.

Hale, W. S., and J. W. Head (1981), Central peaks in Martian craters: Comparisons to the moon and Mercury, *Lunar Planet. Sci.*, *XII*, 386–388.

Head, J. W., III (2000), Extensive south polar ice cap in Middle Mars history? Tests using MOLA data, *Lunar Planet. Sci. Conf.* [CD-ROM], *XXXI*, Abstract 1119.

Head, J. W., and D. R. Marchant (2003), Cold-based mountain glaciers on Mars: Western Arsia Mons, *Geology*, *31*, 641–644.
Head, J. W., et al. (2005), Tropical to mid-latitude snow and ice accumulation, flow and glaciation on Mars, *Nature*, *434*, 346–351.
Head, J. W., D. R. Marchant, M. C. Agnew, C. I. Fassett, and M. A. Kreslavsky (2006), Extensive valley glacier deposits in the northern mid-latitudes of Mars: Evidence for Late Amazonian obliquity-driven climate change, *Earth Planet Sci. Lett.*, *241*, 663–671.
Hooke, R. L. (2005), *Principles of Glacier Mechanics*, Cambridge Univ. Press, Cambridge, U.K.
Hvidberg, C. S. (2002), Investigating timescales for closing polar troughs in the north polar cap on Mars by flow, *Lunar Planet. Sci. Conf.* [CD-ROM], *XXXIII*, Abstract 1669.
Kargel, J. S. (2004), *Mars: A Warmer Wetter Planet*, 557 pp., Praxis-Springer, New York.
Kargel, J. S., and R. G. Strom (1990), Ancient glaciation on Mars, *Lunar Planet. Sci. Conf.*, *XXI*, 597–598.
Kargel, J. S., and R. G. Strom (1992), Ancient glaciation on Mars, *Geology*, *20*, 3–7.
Koutnik, M. R., S. Byrne, B. C. Murray, A. D. Toigo, and Z. A. Crawford (2005), Eolian controlled modification of the Martian south polar layered deposits, *Icarus*, *174*, 490–501.
Li, J., T. H. Jacka, and W. F. Budd (1996), Deformation rates in combined compression and shear for ice which is initially isotropic and after the development of strong anisotropy, *Ann Glaciol.*, *23*, 247–252.
Lliboutry, L. (1979), Local friction laws for glaciers: A critical review and new openings, *J. Glaciol.*, *23*, 67–95.
Mahajan, R. A., R. Greve, and B. Grieger (2004), Effect of dust content and ice rheology on evolution of north polar ice cap of Mars, paper presented at 35th COSPAR Scientific Assembly, Comm. on Space Res., Paris.
McConnell, J. R., R. J. Arthern, E. Mosley-Thompson, C. H. Davis, R. C. Bales, R. Thomas, J. F. Barkhart, and J. D. Kyne (2000), Changes in Greenland ice sheet elevation attributed primarily to show accumulation variability, *Nature*, *406*, 877–879.
Mellon, M. T. (1996), Limits on the CO_2 content of the Martian polar deposits, *Icarus*, *124*, 268–279.
Melosh, H. J. (1989), *Impact Cratering: A Geologic Process*, Oxford Univ. Press, New York.
Moore, H. J., and P. A. Davis (1987), Ablation of Martian glaciers, paper presented at MECA Symposium on Mars: Evolution of Its Climate and Atmosphere, Lunar and Planet. Inst., Houston, Tex.
Nye, J. F. (1951), The flow of glaciers and ice-sheets as a problem in plasticity, *Proc. R. Soc. London, Ser. A*, *207*, 554–570.
Nye, J. F. (1952a), The mechanics of glacier flow, *J. Glaciol.*, *2*, 82–93.
Nye, J. F. (1952b), A method of calculating the thicknesses of the ice-sheets, *Nature*, *169*, 529–530.
Nye, J. F. (2000), A flow model for the polar caps of Mars, *J. Glaciol.*, *46*, 438–444.
Nye, J. F., W. B. Durham, P. M. Schenk, and J. M. Moore (2000), The instability of a south polar cap on Mars composed of carbon dioxide, *Icarus*, *144*, 449–455.
Paterson, W. S. B. (1994), *The Physics of Glaciers*, Pergamon, Oxford, U.K.
Pathare, A. V., D. A. Paige, and E. Turtle (2005), Viscous relaxation of craters within the Martian polar layered deposits, *Icarus*, *174*, 396–418.
Pike, R. J. (1988), Geomorphology of impact craters on Mercury, in *Mercury*, pp. 165–273, Univ. of Ariz. Press, Tucson.
Reeh, N. (1982), A plasticity-theory approach to the steady-state shape of a three-dimensional ice sheet, *J. Glaciol.*, *28*, 431–455.
Reeh, N. (1984), Reconstruction of the ice covers of Greenland and the Canadian Arctic Islands by 3-dimensional, perfectly plastic ice-sheet modeling, *Ann. Glaciol.*, *5*, 115–121.
RIVIX (2005), RiverTools Version 3.0.3 for Windows, computer software, Broomfield, Colo.
Schaller, E. L., B. Murray, A. V. Pathare, J. Rasmussen, and S. Byrne (2005), Modification of secondary craters on the Martian south polar layered deposits, *J. Geophys Res.*, *110*(E2), doi:10.1029/2004JE002334.
Schmidt, K. G., and S. L. Buchardt (2004), Modeling the mass balance of the northern polar ice cap on Mars, *Lunar Planet. Sci. Conf.* [CD-ROM], *XXXV*, Abstract 1554.
Smith, D. E., et al. (1999), The global topography of Mars and implications for surface evolution, *Science*, *284*, 1495–1503.
Thomas, P., S. Squyres, K. Herkenhoff, S. Howard, and B. Murray (1992), Polar deposits on Mars, in *Mars*, edited by H. H. Kieffer et al., pp. 767–795, Univ. of Ariz. Press, Tucson.
Tulaczyk, S., W. B. Kamb, and H. F. Engelhardt (2000), Basal mechanics of Ice Stream B, West Antarctica: 2. Undrained plastic bed model, *J. Geophys. Res.*, *105*(B1), 483–491.
Zwally, H. J., and J. L. Saba (1999), Driving stresses in Mars polar ice caps and conditions for ice flow, paper presented at Fifth International Conference on Mars, Lunar and Planet. Inst., Houston, Tex.

M. E. Banks and J. D. Pelletier, Department of Geosciences, University of Arizona, Gould-Simpson Building 77, 1040 E. 4th Street, Tucson, AZ 85721, USA.